Measurements and Modeling of III–V Solar Cells at High Temperatures up to 400 °C

Emmett E. Perl, John Simon, John F. Geisz, Minjoo Larry Lee, Daniel J. Friedman, and Myles A. Steiner

Abstract—In this paper, we study the performance of 2.0 eV $Al_{0.12}Ga_{0.39}In_{0.49}P$ and 1.4 eV GaAs solar cells over a temperature range of 25–400 °C. The temperature-dependent J_{01} and J_{02} dark currents are extracted by fitting current–voltage measurements to a two-diode model. We find that the intrinsic carrier concentration n_i dominates the temperature dependence of the dark currents, open-circuit voltage, and cell efficiency. To study the impact of temperature on the photocurrent and bandgap of the solar cells, we measure the quantum efficiency and illuminated current–voltage characteristics of the devices up to 400 °C. As the temperature is increased, we observe no degradation to the internal quantum efficiency and a decrease in the bandgap. These two factors drive an increase in the short-circuit current density at high temperatures. Finally, we measure the devices at concentrations ranging from ∼30 to 1500 suns and observe $n = 1$ recombination characteristics across the entire temperature range. These findings should be a valuable guide to the design of any system that requires high-temperature solar cell operation.

Index Terms—III–V and concentrator photovoltaics (PV), PV cells, semiconductor materials, solar energy, temperature dependence.

I. INTRODUCTION

THERE are a number of space and terrestrial applications that would benefit from the development of photovoltaic devices that can operate at high temperatures. For example, a photovoltaic–thermal (PV-T) hybrid solar collector could utilize a high-temperature photovoltaic topping device to simultaneously achieve dispatchability and a high sunlight-to-electricity efficiency [1]–[3]. For even the most efficient solar cells, a significant fraction of incoming solar energy will be converted into heat within the semiconductor [4]–[13]. A hybrid solar converter could transfer this heat from the photovoltaic cell to a thermal collector that could then provide storage and dispatchable energy to the electrical grid using a conventional generator. Fig. 1 shows a schematic diagram of how a high-temperature photovoltaic device could be integrated into a PV-T hybrid solar collector.

A near-sun space mission would also require the development of robust solar cells that remain efficient at elevated temperatures before photovoltaic power generation can be viably considered for these missions. One example is a mission to Mercury, which would require photovoltaic cells to operate at temperatures of about 450 °C and light intensities ∼10× higher than in earth orbit [14], [15].

The development of photovoltaic devices for these applications introduces a number of challenges inherent to high-temperature operation. Raising the operating temperature will increase the J_{01} and J_{02} dark currents exponentially, leading to a significant reduction in the open-circuit voltage (V_{OC}) of a solar cell [4], [5], [12]. High-temperature operation could also accelerate material degradation, reduce long-term reliability, and necessitate the development of a stable metallization and cell encapsulant. These challenges need to be carefully explored and understood before any photovoltaic device can be viably integrated into a system that requires high-temperature operation.

We showed previously that a dual-junction solar cell with room-temperature bandgaps of 2.0 eV for the top junction and 1.4 eV for the bottom junction is nearly optimal for operation at a temperature of 400 °C and a concentration of 1000 suns [16], [17]. In this paper, we study the temperature-dependent cell properties of $Al_{0.12}Ga_{0.39}In_{0.49}P$ (hereafter AlGaInP) and GaAs solar cells with room-temperature bandgaps of 2.0 and 1.4 eV, respectively. Temperature-dependent measurements of these devices are compared with an analytical drift-diffusion model to determine the dominant factors that influence cell performance at elevated temperatures [4], [5], [12].

II. EXPERIMENTAL METHODS

All of the solar cells studied in this study were grown using a custom-built atmospheric pressure organometallic vapor-phase epitaxy (OMVPE) vertical reactor. The samples were grown on zinc-doped (0 0 1) GaAs substrates miscut 6° toward ⟨1 1 1⟩ A. The structure and growth conditions of the AlGaInP cell were discussed in detail previously [16], [17]. The GaAs cell is grown upright and consists of a 300 nm p-type GaInP back surface field (BSF), a 3-μm p-type GaAs base, a 100-nm n-type GaAs emitter, and a 25-nm n-type GaInP window layer. A 1-μm thick n-type AlGaInP layer is grown on top of the GaAs cell to filter out high-energy light that would be absorbed by the AlGaInP subcell of a dual-junction device.
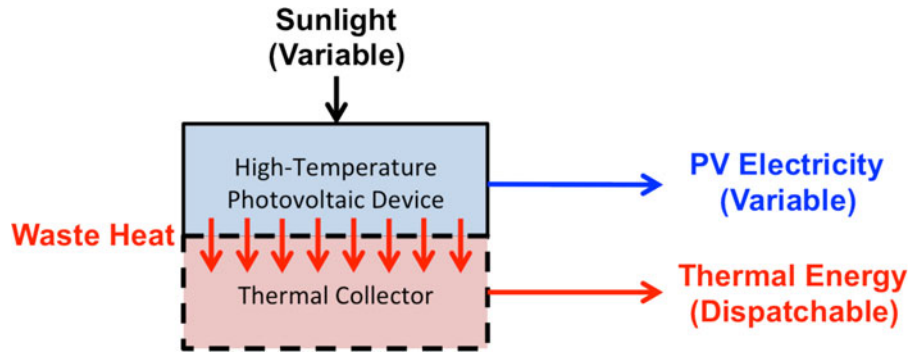
Fig. 1. Diagram showing how a high-temperature photovoltaic topping device could be integrated into a PV-T hybrid solar collector. Energy losses, which are primarily converted into heat, can be transferred to a thermal collector that can drive a conventional generator to provide dispatchable energy to the electrical grid.
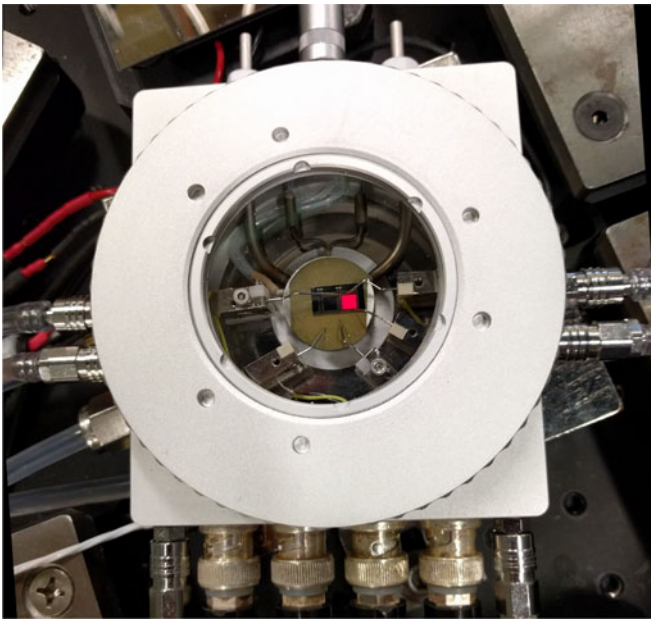

Fig. 2. HFS600E-PB4 Linkam stage used to measure the temperature-dependent characteristics of our solar cells. An AlGaInP cell is being forward biased at 400 °C, leading to a red shift in its EL spectrum (orange light is emitted at room temperature).

Standard photolithography and wet chemical etching techniques were used to process devices with an illuminated area of approximately 0.1 cm^2. We have developed a few candidate high-temperature metallizations in this project. For the AlGaInP cell, we deposited a metal stack consisting of Ti/WTi/Al/Ti (50/50/3000/50 nm) on the front surface of the sample. For the GaAs cell, we deposited a metal stack consisting of Ti/Pt/Al/Pt (50/50/5000/50 nm). We found that these contacts remained stable for the duration of our high-temperature testing, though further work must be done to determine the long-term stability of these metal stacks.

To measure the cell performance at elevated temperatures, we used an HFS600E-PB4 temperature controlled stage built by Linkam Scientific Instruments. This stage, shown in Fig. 2, has the ability to control the sample temperature from 25 to 600 °C and has five sample probes that are used to measure the electrical characteristics of the solar cells. The Linkam stage also

has a 3-in diameter glass window that allows for electro-optical measurements of the devices. All the cells were measured in a nitrogen environment to minimize the risk of oxidizing the AlInP window layer; however, we have recently carried out 200 h anneals at 400 °C and observed that the performance of our solar cells remains stable when encapsulated with a layer of Al_2O_3.

This temperature-controlled stage was incorporated into our quantum efficiency, current–voltage, and flash testing setups to enable temperature-dependent measurements of the cell properties. The window of the Linkam stage reflects ~8% of incoming light, which lowers the number of photons incident on the solar cell. Since accurate quantum efficiency measurements require that the intensity of incident light be carefully calibrated, it is necessary for us to characterize the wavelength-dependent reflectance of this window. In order to correct for the window reflectance (R_{window}), we must divide the external quantum efficiency (EQE) by $(1 - R_{\mathrm{window}})$ and the cell reflectance (R_{cell}) by $(1 - R_{\mathrm{window}})^2$, where the exponent of 2 comes from the two passes that the monochromatic light makes through the window. The internal quantum efficiency (IQE) is calculated from the corrected EQE and cell reflectance using [18]

$$\mathrm{IQE}\,(\lambda) = \frac{\mathrm{EQE}\,(\lambda)}{1 - R_{\mathrm{cell}}\,(\lambda)}. \tag{1}$$

To measure the 1-sun illuminated current–voltage (LIV) and dark current–voltage (DIV) characteristics of our cells, we used a custom-built solar simulator with a Xenon lamp and adjustable high-brightness LEDs. The spectrum and intensity are adjusted using calibrated reference cells to simulate the AM1.5D spectrum at 1000 W/m^2 [19]. When calibrating the 1 sun light intensity for cells in the Linkam stage, it is important to take into account the temperature variation of the EQE curves. To do this, we used calibrated GaInP and GaAs reference cells to calculate a spectral mismatch correction factor at each temperature and added LED light until an equivalent 1 sun intensity was reached [20].

For concentrator measurements, we used the high-intensity pulsed solar simulator (HIPSS) at NREL [20]. This system uses two low-pressure Xenon arc lamps to deliver millisecond-length pulses of light to the cell, enough time to measure the LIV characteristics of our devices. The light intensity is varied from

~30 to ~1500 suns by adjusting the area of an aperture that blocks out a fraction of the light generated by the arc lamps. We assume that the photocurrent varies linearly with intensity, and determine the concentration from the ratio of the short-circuit current density (J_{SC}) measured using the HIPSS to the 1 sun J_{SC} measured using our solar simulator. At the largest apertures and highest temperatures, the series resistance can prevent the LIV curves from flattening before J_{SC}. When this is the case, the J_{SC} cannot be used as an indicator of the concentration. For those curves, we estimate the concentration by assuming that the variation of photocurrent with temperature is the same at all apertures. Therefore, the relative change in photocurrent from 25 to 400 °C should be the same at the largest aperture (>1000 suns) as it is at the smallest aperture (<40 suns), and the concentrations can be appropriately scaled. This assumption will be validated below.

The temperature of the Linkam stage is measured using a thermocouple embedded in the stage. Since our cells are placed on top of the stage, separated from the thermocouple, it is important to verify that the temperature of our devices is close to the thermocouple temperature. To do this, we measured the electroluminescence (EL) spectrum of a GaAs solar cell as the Linkam stage was heated and used the peak emission energy (E_{peak}) as a thermometer for the cell temperature. The bandgap of the GaAs active layers can be calculated by subtracting $kT/2$ from this peak emission energy, where k is the Boltzmann constant and T is the cell temperature in Kelvin [21]. The temperature dependence of the GaAs bandgap can also be described by the Varshni equation shown as [22]

$$E_g(T) = E_g(0) - \frac{\alpha T^2}{T + \beta} = E_{\text{peak}}(T) - \frac{kT}{2} \quad (2)$$

where α and β are material constants and $E_g(0)$ is the bandgap at 0 K. Since the Varshni parameters are well characterized for GaAs ($\alpha = 0.5405$ meV/K, $\beta = 204$ K [23]), we can use this equation to solve for the cell temperature from the peak emission energy of the cell measured using EL. Fig. 3 shows a comparison between the cell temperature calculated using (2) and the thermocouple temperature. The dashed line has a slope of 1 to indicate how far off the cell temperature is from the thermocouple temperature. This plot gives us a good sense for how the thermocouple temperature and the cell temperature differ. On average, we measure a cell temperature that is 5.8 °C higher than the thermocouple temperature, with a standard deviation of 3.6 °C. All temperatures reported in the following sections correspond to the thermocouple temperature.

III. TEMPERATURE-DEPENDENT SOLAR CELL MODEL

The operation of a p-n junction solar cell is often described using the two-diode model shown as [4], [5]

$$J = J_{01}\left(e^{q(V-JR_S)/kT} - 1\right) + J_{02}\left(e^{q(V-JR_S)/2kT} - 1\right)$$
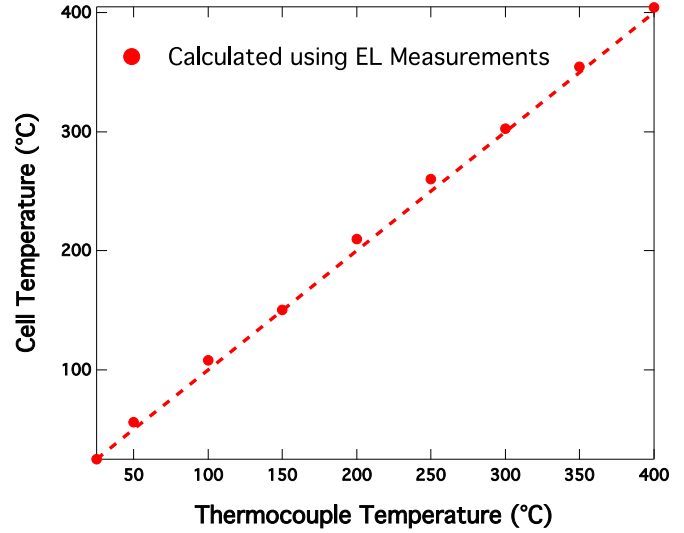$$+ \frac{(V - JR_S)}{R_{\text{shunt}}} - J_L \quad (3)$$

Fig. 3. Comparison between the cell temperatures calculated using (2) and the temperature of the thermocouple embedded in the Linkam stage. The dashed line has a slope of 1 to indicate how far off the cell temperature is from the thermocouple temperature.

where J is the current density of the cell, J_{01} and J_{02} are the dark saturation current densities, q is elementary charge, V is the applied voltage, R_S is the series resistance, R_{Shunt} is the shunt resistance, and J_L is the photocurrent density [5]. This relationship can be used to determine all the relevant performance characteristics of a solar cell, including the V_{OC}, fill factor (FF), and cell efficiency. For this reason, it is critically important to characterize the temperature dependence of J_L, J_{01}, and J_{02} in order to understand how cell performance will be impacted as the operating temperature is varied.

The analytical drift-diffusion model splits the dark currents into three components corresponding to recombination in the emitter, base, and depletion regions. The J_{01} dark saturation current densities, arising from bulk and interface recombination in the quasi-neutral emitter and base regions, are defined as follows [4], [5], [12]:

$$J_{01,\,\text{emitter}} = q\left[\frac{D_p}{L_p}\right]\left[\frac{n_i^2}{N_D}\right]$$
$$\times \left[\frac{\frac{S_p L_p}{D_p}\left(\cosh\left(\frac{x_e}{L_p}\right)\right)^2 + \sinh\left(\frac{x_e}{L_p}\right)}{\frac{S_p L_p}{D_p}\sinh\left(\frac{x_e}{L_p}\right) + \cosh\left(\frac{x_e}{L_p}\right)}\right] \quad (4)$$

$$J_{01,\text{base}} = q\left[\frac{D_n}{L_n}\right]\left[\frac{n_i^2}{N_A}\right]$$
$$\times \left[\frac{\frac{S_n L_n}{D_n}\left(\cosh\left(\frac{x_b}{L_n}\right)\right)^2 + \sinh\left(\frac{x_b}{L_n}\right)}{\frac{S_n L_n}{D_n}\sinh\left(\frac{x_b}{L_n}\right) + \cosh\left(\frac{x_b}{L_n}\right)}\right] \quad (5)$$

where D_p is the diffusion constant for minority carriers in the n-type emitter, D_n is the diffusion constant for minority carriers in the p-type base, L_p is the minority carrier diffusion length in the emitter, L_n is the minority carrier diffusion length in the base, S_p is the surface recombination velocity at the emitter–window interface, S_n is the surface recombination velocity at

the base–BSF interface, N_A is the acceptor concentration in the base, N_D is the donor concentration in the emitter, x_b is the base thickness, x_e is the emitter thickness, and n_i is the intrinsic carrier concentration.

The J_{02} dark saturation current density, arising from nonradiative recombination in the depletion region, is described by [4], [5], [12]

$$J_{02,\,\text{depletion}} = \frac{q n_i W_d}{2\tau} \tag{6}$$

where W_d is the width of the depletion region and τ is the nonradiative carrier lifetime in the material.

The intrinsic carrier concentration n_i is the dominant factor in (4)–(6) that will determine the temperature dependence of the dark currents, and is defined according to [24]

$$n_i(T) = 2\left(\frac{2\pi kT}{h^2}\right)^{3/2}(m_n{}^* m_p{}^*)^{3/4} e^{-E_g/2kT} \tag{7}$$

where E_g is the bandgap, h is Planck's constant, $m_n{}^*$ is the effective electron mass, and $m_p{}^*$ is the effective hole mass.

Combining (4)–(6) with (7), we find that the n_i-dominated temperature dependence of the J_{01} and J_{02} dark currents can be described by the following proportionalities:

$$J_{01} \;\; \alpha \;\; T^3 e^{-E_g/kT} \tag{8}$$

$$J_{02} \;\; \alpha \;\; T^{3/2} e^{-E_g/2kT}. \tag{9}$$

These equations indicate that the J_{01} and J_{02} dark currents will increase exponentially with temperature, which will lead to a significant reduction in the V_{OC} at high temperatures.

The photocurrent is closely linked to the EQE of the cell, which can also be split into three components corresponding to collection in the emitter, base, and depletion regions. While these equations can be solved to obtain expressions for the EQE in each region, the solutions are quite complex and there is no single term that will dominate the temperature dependence [4], [5], [12].

IV. Cell Results and Discussion

Here, we describe quantum efficiency, current–voltage, and concentrator measurements of AlGaInP and GaAs solar cells taken over a temperature range of 25–400 °C. Our results are compared with the temperature-dependent solar cell model detailed in the previous section.

A. Temperature-Dependent Performance of the AlGaInP Cell

The temperature-dependent IQE of the AlGaInP cell is shown in Fig. 4. There are two main takeaways from this plot. First, the IQE does not degrade significantly as the cell temperature is increased, with the magnitude of the peak IQE remaining at ∼86% over the entire temperature range. Second, the bandgap of the cell decreases from ∼2.01 eV at 25 °C to ∼1.83 eV at 400 °C. Note that the bandgap of the AlInP window layer decreases with temperature as well, leading to a drop in the short-wavelength IQE.

Fig. 5 shows temperature-dependent LIV measurements of the AlGaInP solar cell taken at 1000 W/m² (1 sun) under the
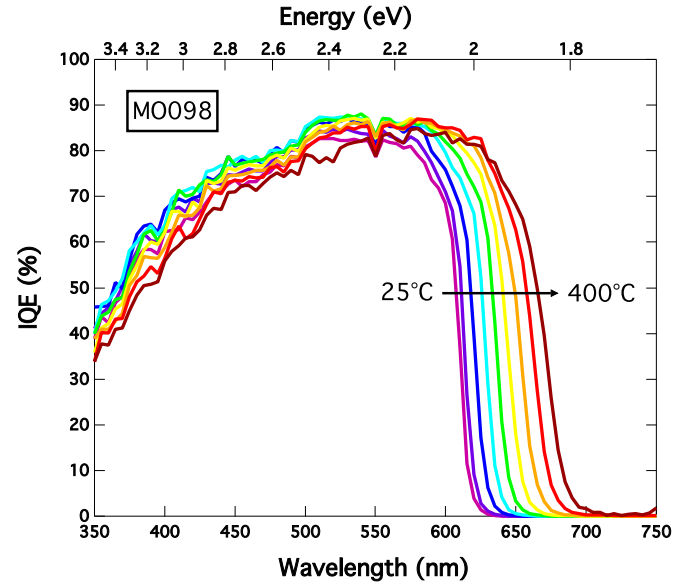

Fig. 4. Temperature-dependent IQE of the AlGaInP solar cell showing no significant degradation to the peak IQE and a reduction in the bandgap of the AlInP window and AlGaInP active layers as the temperature is increased. These two factors drive an increase in the photocurrent at high temperatures.
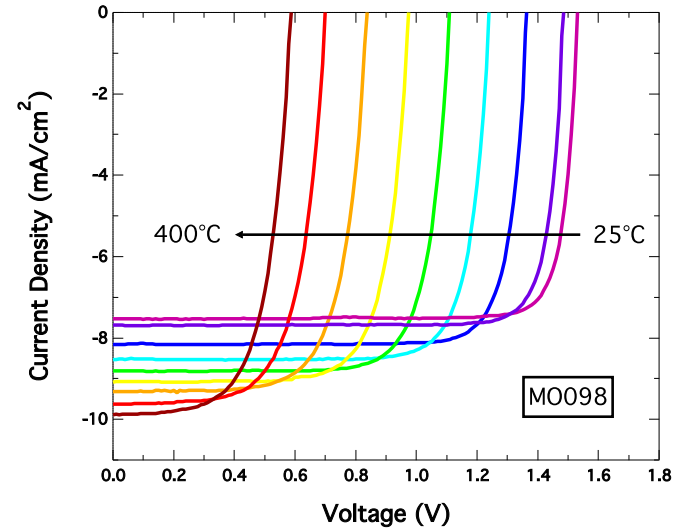

Fig. 5. Temperature-dependent LIV measurements of the AlGaInP solar cell taken at a light intensity of 1 sun under the AM1.5D spectrum. As the temperature is increased, we observe an increase in J_{SC} and decrease in V_{OC}.

AM1.5D spectrum. We observe a small increase in the J_{SC} at high temperatures due to the decreasing bandgap of AlGaInP. We also find that the V_{OC} decreases at a rate of ∼2.6 mV/°C over this temperature range at a light intensity of 1 sun. The dominant factor impacting the cell efficiency is the decreasing V_{OC}, which is a direct result of the exponentially increasing J_{01} and J_{02} dark currents.

Temperature-dependent DIV measurements of the AlGaInP solar cell are shown in Fig. 6. At low voltages ($V < 100$ mV), the curves bend downward because of the −1 terms in the diode equations. At high currents ($J > 100$ mA/cm²), the curves begin to roll over due to series resistance. The dashed lines on this
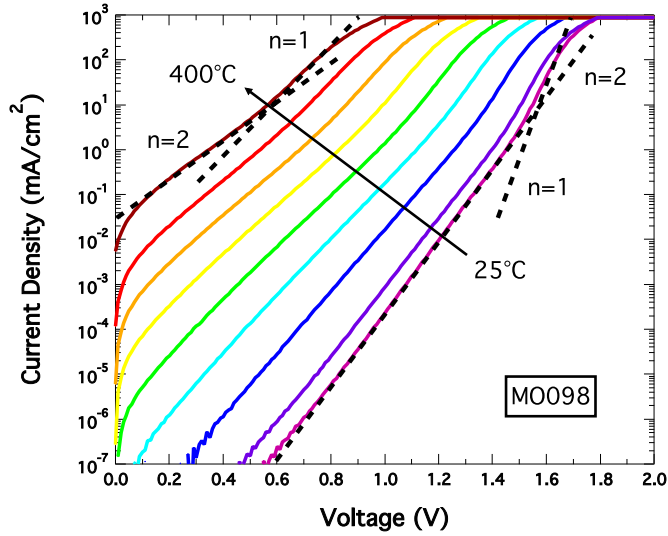
Fig. 6. Temperature-dependent DIV measurements of the AlGaInP solar cell showing an increase in the J_{01} and J_{02} dark currents as the temperature is increased. The dashed lines indicate the slopes of ideal diodes with ideality factors of 1 and 2, at temperatures of 25 and 400 °C.

Fig. 7. Comparison between the dark currents extracted from temperature-dependent DIV measurements and the n_i dependence of the dark currents calculated using (8) and (9) for the AlGaInP cell.

plot indicate the slopes of ideal diodes with ideality factors of 1 and 2, at temperatures of 25 and 400 °C. Note that these slopes change with temperature because of the kT/q arguments in the exponents of (3). The *y*-intercepts of these lines correspond to J_{01} for the $n = 1$ line and J_{02} for the $n = 2$ line. For this AlGaInP cell, there are clear $n = 1$ and $n = 2$ regions at every temperature measured, allowing us to extract the temperature-dependent J_{01} and J_{02} dark currents. We compare these values to the n_i dependence of the dark currents shown in (8) and (9).

When calculating the temperature dependence of the dark currents from these equations, we use values for J_{01} and J_{02} extracted at room temperature as a starting point and extrapolate these values to 400 °C with (8) and (9). The temperature dependence of the bandgap $E_g(T)$ is derived from the EL measurements detailed in Section II. Fig. 7 shows a comparison between the dark currents extracted from the DIV measurements of Fig. 6 and the n_i dominated temperature dependence of the dark currents calculated from (8) and (9). The excellent agreement between the dark currents extracted from DIV measurements and the dark currents calculated using (8) and (9) provides evidence that the recombination characteristics that are described by (4)–(6) continue to remain valid at temperatures as high as 400 °C for the AlGaInP solar cell. It also confirms that the intrinsic carrier concentration n_i is the dominant term that impacts the temperature dependence of the dark currents.

Flash measurements of the AlGaInP cell, taken using the HIPSS, are shown in Fig. 8. Due to the relatively high R_s of this AlGaInP cell, we observe a drop in the FF at all temperatures when the intensity of light is increased above 1000 suns. For the flash measurements taken at 400 °C, the FF drops from ~71% at 40 suns to ~48% at 1200 suns. Although we have not yet made a significant effort to reduce this series resistance, we expect that we can achieve a better FF at high concentration with an improved grid design and a reduction in the emitter sheet resistance.
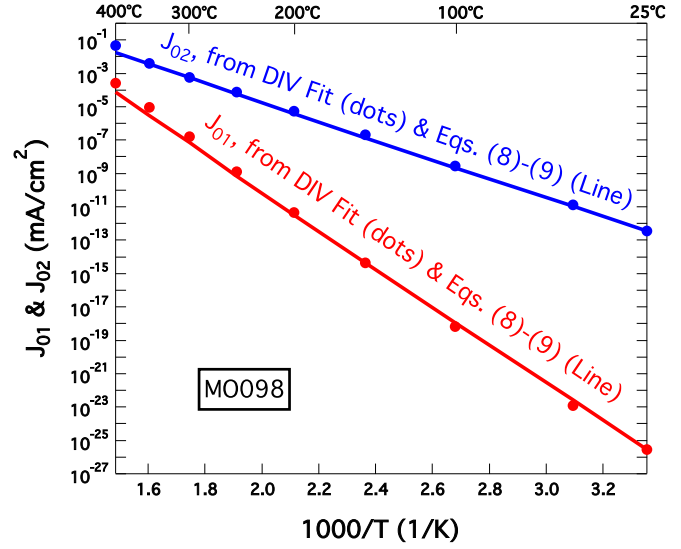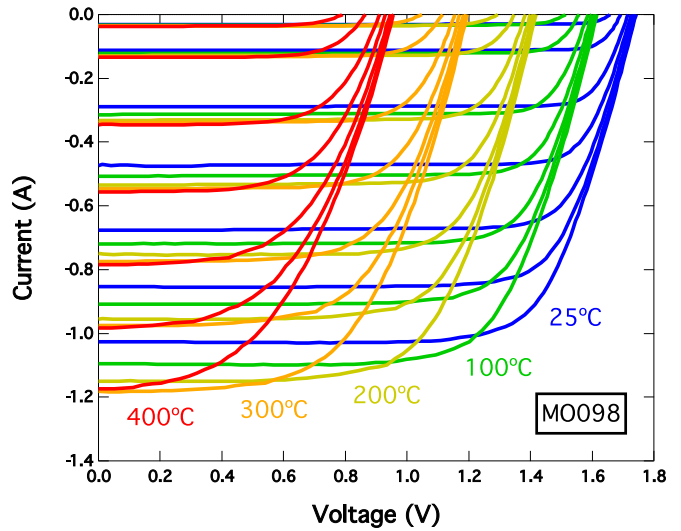

Fig. 8. Flash measurements of the AlGaInP solar cell taken using the HIPSS at seven different apertures. The light intensities range from less than 40 suns at the smallest aperture to over 1000 suns at the largest aperture.

For the measurements taken at 400 °C, we cannot determine the concentration from the measured J_{SC} at the four largest apertures (>500 suns) because series resistance prevents the LIV curves from flattening before J_{SC}. For these curves, we estimate the concentration of light using the procedure described in Section II. To validate this procedure, we compared the ratio of J_{SC} at high temperatures (100, 200, 300, 400 °C) with the room temperature J_{SC} at each aperture for the curves that flatten before J_{SC}, and we measure a standard deviation of 0.8% from the average between these ratios. This supports our previous assumption that the linearity of the current versus light intensity is not changing significantly as we increase the temperature from 25 to 400 °C.
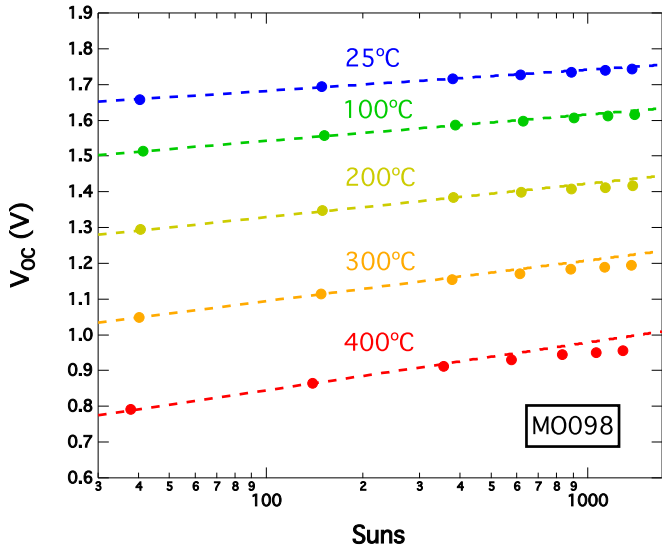
Fig. 9. V_{OC} as a function of both temperature and concentration for the AlGaInP solar cell. The dashed lines show the slopes of these curves for an ideal $n = 1$ diode at each temperature.

Fig. 9 shows a plot of the V_{OC} of the AlGaInP cell, measured using the HIPSS, as a function of both temperature and concentration. At a temperature of 400 °C, the V_{OC} increases from ~600 mV at 1 sun to ~950 mV at 1000 suns. The dashed lines show the slopes of these curves for an ideal $n = 1$ diode at each temperature. The overlap of this line with our measured data shows that there is a clear $n = 1$ region at lower concentrations; however, the V_{OC} starts to roll over at increasing concentrations. We are still investigating the cause of this rolloff. Note also that the slopes of the $n = 1$ lines increase with temperature, due to the increasing kT/q arguments in the exponents of (3). This suggests that moving to high concentration is even more leveraging at high temperatures than it is at room temperature.

B. Temperature-Dependent Performance of the GaAs Cell

The temperature-dependent IQE of the filtered GaAs cell is shown in Fig. 10. Similar to what we observed with the AlGaInP cell, there is no significant degradation to the IQE as the cell temperature is increased, with the magnitude of the peak IQE remaining at ~92% over the entire temperature range. It is also apparent that the bandgap of the GaAs cell and the AlGaInP filter are both decreasing as the temperature is increased, causing the turn-on and turn-off of the IQE curves to shift to longer wavelengths.

Fig. 11 shows temperature-dependent LIV measurements of the GaAs solar cell taken at 1 sun under the AM1.5D spectrum. As the temperature is raised, we observe an increase in J_{SC} due to the decreasing bandgap of GaAs. It is also clear that there is a significant slope at J_{SC} at the highest temperatures, which was not observed for the AlGaInP cell. The reason for this is that the dark currents in the lower bandgap GaAs cell are ~100× higher than in the AlGaInP cell at 400 °C. We find that the V_{OC} is decreasing at a rate of ~2.4 mV/°C at a light intensity of 1 sun, and again this is the dominant factor impacting cell efficiency. This cell is clearly not suitable for 1 sun operation at 400 °C
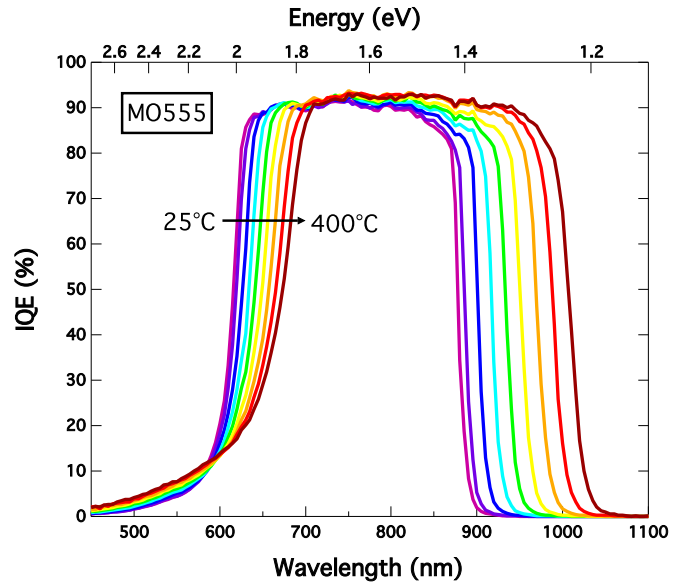

Fig. 10. Temperature-dependent IQE of the GaAs solar cell showing no significant degradation to the peak IQE and a reduction in the bandgap of the AlGaInP filter and the GaAs active layers as the temperature is increased.
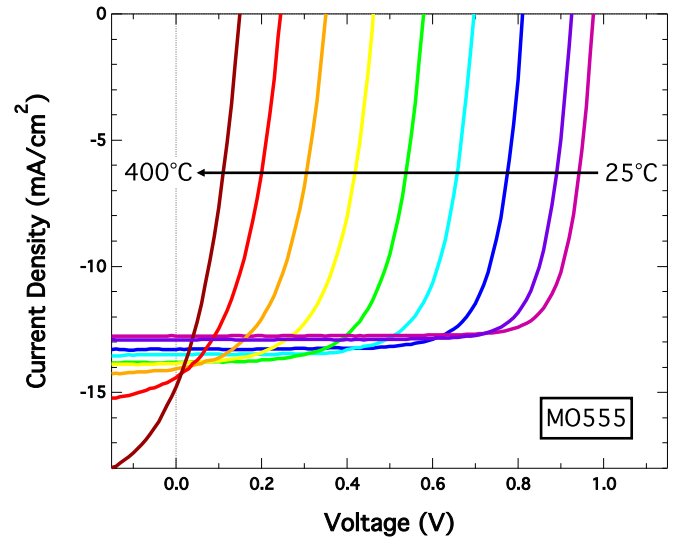

Fig. 11. Temperature-dependent LIV measurements of the GaAs solar cell taken at a light intensity of 1 sun under the AM1.5D spectrum. As the temperature is increased, we observe an increase in J_{SC} and decrease in V_{OC}.

due to its low V_{OC} and the large slope at J_{SC}. However, as the concentration is increased, the V_{OC} will increase significantly and, provided that the R_S is low, the slope at J_{SC} will become insignificant.

Temperature-dependent DIV measurements of the GaAs solar cell are shown in Fig. 12. The dashed lines on this plot indicate the slopes of ideal diodes with ideality factors of 1 and 2 at a temperature of 25 °C. As with the AlGaInP cell, there is a clear $n = 2$ region at every temperature measured, allowing us to extract the temperature-dependent J_{02} dark current. However, we were unable to fit to the $n = 1$ line at the highest temperatures, and therefore, the J_{01} dark currents must instead be extracted using concentrator measurements.
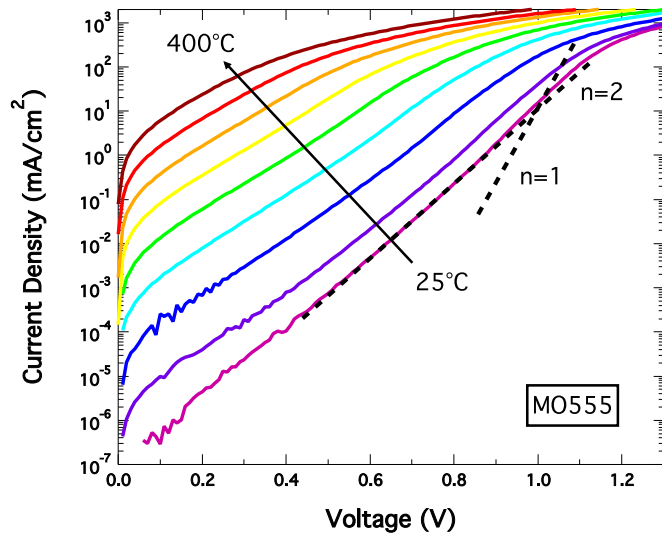
Fig. 12.   Temperature-dependent DIV measurements of the GaAs solar cell showing an increase in the J_{02} dark currents as the temperature is increased. The dashed lines indicate the slopes of ideal diodes with ideality factors of 1 and 2 at a temperature of 25 °C.

Fig. 14. $V_{\rm OC}$ as a function of both temperature and concentration for the GaAs solar cell. The dashed lines show the slopes of these curves for an ideal $n = 1$ diode at each temperature and can be used to extract the temperature-dependent J_{01} dark currents.
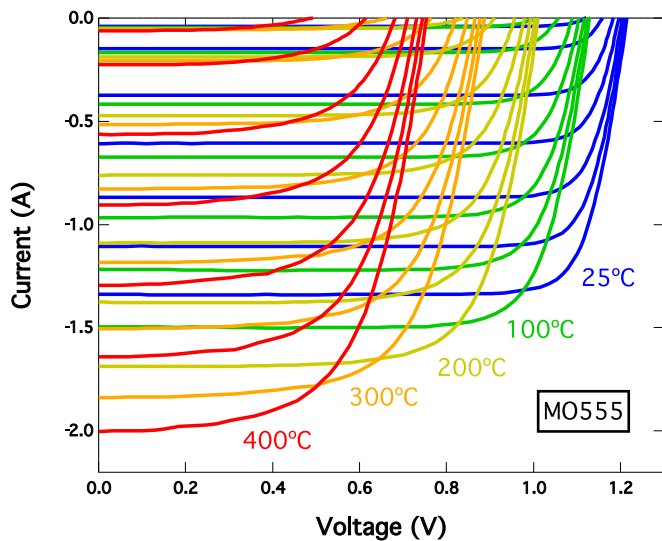

Fig. 13.   Flash measurements of the GaAs solar cell taken using the HIPSS at seven different apertures. The light intensities range from less than 40 suns at the smallest aperture to over 1000 suns at the largest aperture.

Fig. 15.   Comparison between the J_{01} dark currents extracted from temperature-dependent flash measurements, the J_{02} dark currents extracted from DIV measurements, and the n_i dependence of the dark currents calculated using (8) and (9) for the GaAs cell.

Temperature-dependent flash measurements of the GaAs solar cell are shown in Fig. 13. This sample maintained an excellent FF, >60%, at a concentration of 1000 suns and temperature of 400 °C. Additionally, the low R_S made it possible for every single LIV curve to flatten before $J_{\rm SC}$. We again compared the ratio of the high-temperature $J_{\rm SC}$ with the room temperature $J_{\rm SC}$ at each aperture, and the standard deviation between these ratios was 1.0%, further supporting our previous assumption of linearity of the current versus light intensity.

Fig. 14 shows a plot of the $V_{\rm OC}$ of the GaAs cell as a function of both temperature and concentration, where the dashed lines show the slopes of these curves for an ideal $n = 1$ diode at each temperature. It is clear from these plots that the GaAs cell becomes dominated by $n = 1$ recombination at high light
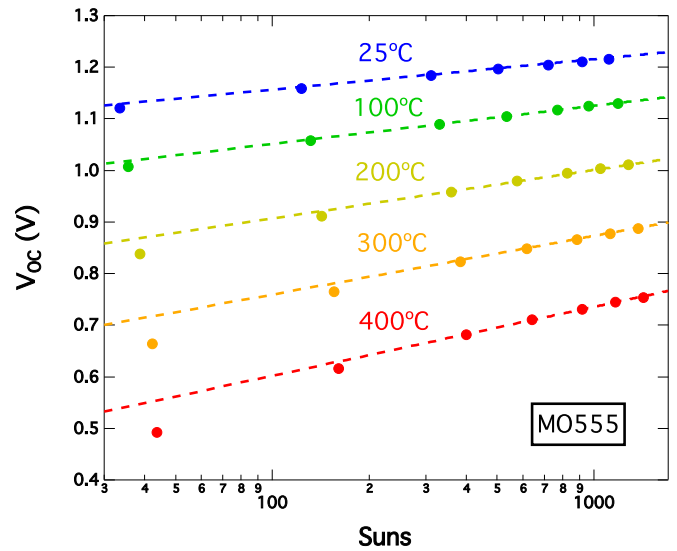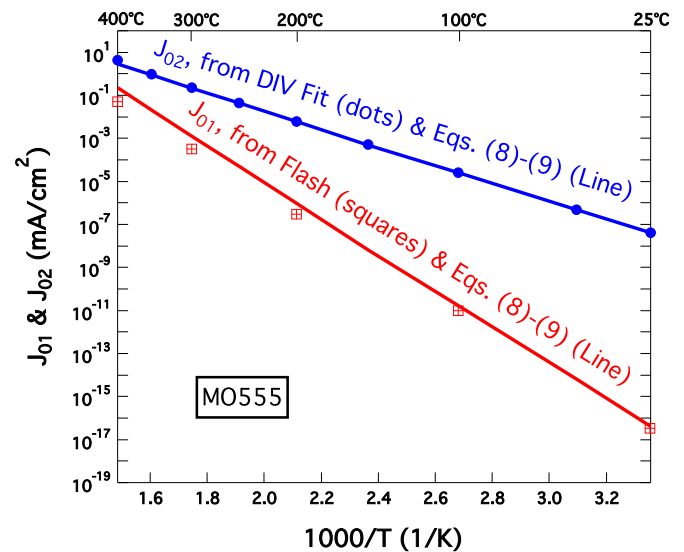
intensities; however, this does not occur until a concentration of 200–300 suns is achieved for the cells measured above 200 °C. These plots also illustrate the significant improvement in the $V_{\rm OC}$ at 400 °C that occurs when these cells are taken to high concentrations. At a temperature of 400 °C, the $V_{\rm OC}$ increases from ∼150 mV at 1 sun to ∼740 mV at 1000 suns. Under the assumption that J_{02} is negligible at these conditions, and that $J = R_S = 0$ at $V_{\rm OC}$, we are able to rearrange (3) to solve for J_{01}

$$J_{01} = \frac{J_L}{e^{qV_{\rm OC}/kT}}. \tag{10}$$

This equation enables us to extract the temperature-dependent J_{01} dark saturation currents from the data in Fig. 14. Fig. 15 shows a comparison between the J_{01} dark currents extracted

from concentrator measurements, the J_{02} dark currents extracted from DIV measurements, and the J_{01} and J_{02} dark currents calculated using (8) and (9). It is clear from this plot that the intrinsic carrier concentration n_i dominates the temperature dependence of the dark currents for the GaAs cell, similar to our findings for the AlGaInP cell. The small deviation in J_{01} the curve at high temperatures could arise from the temperature dependence of the other factors in (4) and (5), and further investigations of these temperature dependencies could enable a higher voltage design at elevated temperatures.

V. CONCLUSION

In this paper, we characterize the performance of AlGaInP and GaAs solar cells over a temperature range of 25–400 °C. We extract the temperature-dependent J_{01} and J_{02} dark currents by fitting DIV and flash measurements to a two-diode model, and find that the intrinsic carrier concentration n_i dominates the temperature dependence of the dark currents for both cells. We take quantum efficiency and LIV measurements to determine the temperature dependence of the photocurrent and bandgap of the devices. We find that there is no significant degradation to the IQE at elevated temperatures, and observe a decrease in the bandgap of our materials. These two factors drive an increase in the photocurrent of both the AlGaInP and GaAs cells. Finally, we measure the devices at high concentrations using the HIPSS, and observe $n = 1$ behavior across the entire temperature range. The findings of this study can be used as a guide to the design of any system that requires solar cell operation at elevated temperatures.

REFERENCES

[1] H. M. Branz, W. Regan, K. Gerst, J. B. Borak, and E. A. Santori, "Hybrid solar converters for maximum energy and inexpensive dispachable energy," *Energy Environ. Sci.*, vol. 8, no. 11, pp. 3083–3091, 2015.

[2] Y. Vorobiev, J. Gonzalez-Hernandez, P. Vorobiev, and L. Bulat, "Thermal photovoltaic solar hybrid system for efficient solar energy conversion," *Sol. Energy*, vol. 80, no. 2, pp. 170–176, 2006.

[3] T. T. Chow, "A review on photovoltaic/thermal hybrid solar technology," *Appl. Energy*, vol. 87, no. 2, pp. 365–379, 2010.

[4] A. L. Fahrenbruch and R. H. Bube, *Fundamentals of Solar Cells*. New York, NY, USA: Academic, 1983, pp. 69–104.

[5] H. J. Hovel, "Solar cells," in *Semiconductors and Semimetals*, vol. 11, R. K. Willardson and A. C. Beer, Eds. New York, NY, USA: Academic, 1975.

[6] J. C. C. Fan, "Theoretical temperature dependence of solar cell parameters," *Solar Cells*, vol. 17, nos. 2/3, pp. 309–315, 1986.

[7] P. Singh, S. N. Singh, M. Lal, and M. Husain, "Temperature dependence of I-V characteristics and performance parameters of silicon solar cells," *Sol. Energy Mater. Sol. Cells*, vol. 92, no. 12, pp. 1611–1616, 2008.

[8] P. Singh and N. M. Ravindra, "Temperature dependence of solar cell performance-an analysis," *Sol. Energy Mater. Sol. Cells*, vol. 101, pp. 36–45, 2012.

[9] D. J. Friedman, "Modeling of tandem cell temperature coefficients," in *Proc. IEEE 25th Photovolt. Spec. Conf.*, 1996, pp. 89–92.

[10] D. Meneses-Rodriguez, P. P. Horley, J. Gonzalez-Hernandez, Y. Vorobiev, and P. N. Gorley, "Photovoltaic solar cells performance at elevated temperatures," *Sol. Cells*, vol. 78, no. 2, pp. 243–250, 2005.

[11] W. Shockley and H. J. Queisser, "Detailed balance limit of efficiency of p-n junction solar cells," *J. Appl. Phys.*, vol. 32, no. 3, pp. 510–519, 1961.

[12] S. R. Kurtz *et al.*, "Passivation of interfaces in high-efficiency photovoltaic devices," presented at the Materials Research Society's Spring Meeting, San Francisco, CA, USA, 1999.

[13] L. C. Hirst and N. J. Ekins-Daukes, "Fundamental losses in solar cells," *Prog. Photovolt., Res. Appl.*, vol. 19, no. 3, pp. 286–293, 2011.

[14] G. A. Landis, D. Merritt, R. Raffaelle, and D. Scheiman, "High-temperature solar cell development," in *Proc. 18th Space Photovolt. Res. Technol. Conf.*, 2005, pp. 241–247.

[15] O. V. Sulima *et al.*, "High-temperature AlGaP/GaP solar cells for NASA space missions," in *Proc. 3rd World Conf. Photovolt. Energy Convers.*, 2003, pp. 737–740.

[16] E. E. Perl *et al.*, "Development of a 2.0 eV AlGaInP solar cell grown by OMVPE," in *Proc. 42nd IEEE Photovolt. Spec. Conf.*, 2015, pp. 1–6.

[17] E. E. Perl *et al.*, "Development of high-bandgap AlGaInP solar cells grown by organometallic vapor-phase epitaxy," *IEEE J. Photovolt.*, vol. 6, no. 3, pp. 770–776, May 2016.

[18] D. J. Friedman, J. M. Olson, and S. R. Kurtz, "High-efficiency III-V multijunction solar cells," *Handbook of Photovoltaic Science and Engineering*, 2nd ed., A. Luque and S. Hegedus, Eds. Chichester, U.K., Wiley, 2011, pp. 314–364.

[19] M. A. Steiner *et al.*, "Temperature-dependent measurements of an inverted metamorphic multijunction (IMM) solar cell," in *Proc. 37th Photovolt. Spec. Conf.*, 2011, pp. 002527–002532.

[20] K. Emery *et al.*, "Procedures for evaluating multijunction concentrators," in *Proc. IEEE 28th Photovolt. Spec. Conf.*, 2000, pp. 1126–1130.

[21] J. I. Pankove, *Optical Processes in Semiconductors*. Chelmsford, MA, USA: Courier, 2012.

[22] Y. P. Varshni, "Temperature dependence of the energy gap in semiconductors," *Physica E, Low-Dimensional Syst. Nanostruct.*, vol. 34, no. 1, pp. 149–154, 1967.

[23] J. S. Blakemore, "Semiconducting and other major properties of gallium arsenide," *J. Appl. Phys.*, vol. 53, no. 10, pp. R123–R181, 1982.

[24] B. G. Streetman and S. Banerjee, *Solid State Electronic Devices*, vol. 5. Englewood Cliffs, NJ, USA: Prentice-Hall, 2000.

Authors' photographs and biographies not available at the time of publication.